
Unravelling the root zone of ultramafic- hosted black smokers- like hydrothermalism from an Alpine analog

Coltat Rémi ^{1,*}, Branquet Yannick ^{1,2}, Gautier Pierre ¹, Campos Rodriguez Hector ¹, Poujol Marc ¹, Pelleter Ewan ³, McClenaghan Sean ^{4,5}, Manatschal Gianreto ⁶, Boulvais Philippe ¹

¹ Univ Rennes, CNRS, Géosciences Rennes - UMR 6118 Rennes, France

² Institut des Sciences de la Terre d'Orléans, UMR 7327, Université Orléans Orléans, France

³ IFREMER, Centre de Brest DRO/GM Plouzané, France

⁴ Department of Geology, Trinity College Dublin Dublin, Ireland

⁵ Irish Centre for Research in Applied Geosciences, Dublin, Ireland

⁶ Institut de Physique du Globe de Strasbourg EOST-CNRS UMR 7516 Université de Strasbourg Strasbourg, France

* Corresponding author : Rémi Coltat, email address : remi.coltat@univ-rennes1.fr

Abstract :

Mid-Ocean Ridges host various types of hydrothermal systems including high-T black-smokers found in ultramafic rocks exhumed along slow spreading ridges. These systems are mostly described in two dimensions as their exposure on the present-day seafloor lacks the vertical dimension. One way to understand these systems at depth is to study their fossilized equivalents preserved on-land. Such observation can be done in the Platta nappe, Switzerland, where a Jurassic-aged mineralized system is exposed in 3D. Serpentinites host a Cu-Fe-Ni-Co-Zn-rich mineralization made of sulphides, magnetite and Fe-Ca-silicates either replacing serpentinites or within stockwork. Fe-Ca-silicates, abundant at the deepest levels, vanish in the mineralization close to the palaeo-detachment. Fluids were channelized along mafic dykes and sills acting as preferential drains. Warm carbonation (~130°C) is the latest hydrothermal record. We propose that this system is an analog to the root zone of present-day serpentinite-hosted hydrothermal systems such as those found along the Mid-Atlantic Ridge.

28 Mid-Ocean Ridges (MORs) are places where deformation-assisted fluid-rock
29 interactions play an important role in elemental mobility (Rona and Scott, 1993). At
30 (ultra)slow-spreading ridges where mantle exhumation is favored by the presence of
31 detachment faults (i.e. oceanic core complexes; Tucholke *et al.*, 1998), these interactions lead
32 to serpentinization of peridotite, venting of hydrothermal fluids with related mineralization,
33 and opihicalcification.

34 Active ultramafic-hosted black-smoker systems (UHS) are characterized by a Cu-Co-Zn-Au-
35 (Ni) enrichment and high contents in CH₄ and H₂ in the venting fluid (Charlou *et al.*, 2002).
36 At the Mid-Atlantic Ridge (MAR), these UHS have been described for two decades through
37 mineralogical (Hannington *et al.*, 1995; Marques *et al.*, 2006), geochemical (Herzig *et al.*,
38 1998; Douville *et al.*, 2002) and tectonic studies (McCaig *et al.*, 2007; McCaig *et al.*, 2010).
39 However, due to restricted access to the seafloor, the understanding of their hydrothermal
40 plumbing system, especially the root zone, (i.e. the mineralized portion below the seafloor)
41 remains limited and speculative (Fouquet *et al.*, 2010) (Fig. 1).

42 Ocean-Continent Transitions (OCTs) display similarities with oceanic realms: mantle
43 exhumation along detachment faults (Boillot *et al.*, 1987), presence of mafic magmatism and
44 high geothermal gradients. Hence, fossil OCTs found in orogenic belts are promising targets
45 to study oceanic hydrothermal processes (e.g. Alt *et al.*, 2018). Here we present the
46 geometric, mineralogical, geochemical and geochronological characteristics of a serpentinite-

47 hosted hydrothermal system now exposed in the Platta nappe (Fig. 2, 3). We propose that this
48 system, active during the Jurassic, represents the root zone of a UHS similar to those found
49 along the MAR.

50 **Geological setting**

51 The Platta nappe (Grisons, SE Switzerland) exposes the Jurassic OCT of the Adriatic
52 plate and belongs to the South Pennine Alpine units (Fig. 2A). Jurassic mantle exhumation
53 was accommodated along detachments faults (Froitzheim and Manatschal, 1996) and
54 accompanied by mafic magmatism (Fig. 2B; Desmurs *et al.*, 2002) dated at 161 ± 1 Ma (U-Pb
55 on zircon; Schaltegger *et al.*, 2002). Evidence of hydrothermal circulation is recorded through
56 alteration of mafic rocks (e.g. rodingitization and epidotization), formation of ultramafic-
57 hosted mineralized systems (e.g. Marmorera-Cotschen, Fig. 3) and opicalcitization (Coltat *et*
58 *al.*, 2019). The end of the rifting phase is marked by deposition of the Radiolarian Chert
59 Formation dated between 166 and 147 Ma (Bill *et al.*, 2001). During the Cretaceous, tectonic
60 inversion triggered the subduction of the Tethyan realm and subsequent continental collision
61 resulting in thickening through W-NW-vergent nappe stacking (D1 phase, Froitzheim *et al.*,
62 1994). The Platta nappe was only affected by a low-temperature prehnite-pumpellyite
63 metamorphism ($< 300^\circ\text{C}$; Dunnoyer de Segonzac and Bernoulli, 1976; Ferreiro-Mahlmänn,
64 1994). During the Cenozoic, N-S-oriented shortening (D3 phase) resulted in the formation of
65 large-scale E-W folds and N-vergent thrusts (Epin, 2017).

66 **Sampling and methods**

67 The serpentinite-hosted mineralization is exposed along the Marmorera-Cotschen cliff
68 (~600m-high; Fig. 3A) where detailed structural mapping and petro-structural analyses have
69 been carried out. The Snake Pit outcrop is close to the paleo-detachment plane (Fig. 3B). A

70 total of 75 thin sections and 9 polished mounts have been prepared from samples
71 representative of the various hydrothermal assemblages: host serpentinites, Fe-Ca-silicates,
72 semi-massive sulfides, Cu-rich massive sulfides (Cu-rich MS) and opicalcites.

73 **Results**

74 **Geometry of the mineralized zones**

75 The Marmorera Cotschen Hydrothermal Systems (MCHS) is hosted in the
76 serpentinitized footwall of a top-to-the-W Jurassic detachment that juxtaposes basalts onto
77 serpentinites (Epin, 2017); the basalts being altered to a greenschist assemblage at their base
78 (Fig. 3A, B). The mineralization occurs along the cliff as sporadic thin oxidized reddish
79 corridors and patches (Fig. 3A, B). It reaches its maximum width at the gossan structure (i.e.
80 oxidized zone after primary sulfides) of Cotschen (Fig. 3B). Mineralization is locally spatially
81 associated with highly altered mafic dyke-like intrusions oriented sub-parallel to the
82 detachment (Fig. 3C-F). Moving away from the intrusions, host serpentinites show a
83 petrographic zonation: Cu-rich massive to semi-massive sulfides evolve toward Fe-Ca-
84 silicates stockwork and pervasive replacement and then to barren serpentinite (Fig. 3E, 4).
85 Close to the detachment, the mineralized serpentinite is crosscut by calcite veins.

86 Alpine deformation is marked by an almost flat N-vergent major thrust (i.e. D3 phase)
87 responsible for the steepening of the former Jurassic detachment and nearby mineralization
88 (Fig. 3A). Minor N-vergent faults occur within the mineralized bodies (Fig. 3F).

89 **Mineralogy and geochemistry of MCHS**

90 Detailed paragenetic sequences are presented in Table S1-1 and summarized in Table
91 1. See also Dietrich (1972). Chemical composition of selected mineralized phases (EPMA
92 analyses) is given in Table S2-1 and S2-2. We first describe the sequence of the

93 mineralization in the most mineralized zones, then the one of the Snake Pit outcrop, close to
94 the detachment plane.

95 Lizardite is the serpentine polymorph forming serpentinite. Small magnetite and pentlandite
96 grains ($< 100\mu\text{m}$) occur along former olivine grain boundaries or within serpentine domains,
97 respectively (Fig. 4A). Magnetite is commonly found in replacement after Cr-spinel.

98 Pentlandite is characterized by high Ni (35.84 to 36.14 wt.%) and low Co (1.66 to 1.80 wt.%)
99 contents (with Co/Ni ratio ~ 0.05 , Fig. 5A). Magnetite displays high Si contents (0.43 to 1.26
100 wt.%; Fig. 5B).

101 Toward the mineralized zones, lizardite is progressively replaced by Fe-antigorite/greenalite.
102 Serpentinites are crosscut by Fe-Ca-silicates veins comprised of ilvaite, hydro-andradite and
103 Fe-diopside ($\text{Di}_{21}\text{-Di}_{84}$), associated with fibrous Fe-antigorite/greenalite, defining a stockwork
104 structure (Fig. 4B-D). Locally, the amount of Fe-Ca-silicates increases drastically and they
105 massively replace serpentinites along metasomatic bands (Fig. 4E). Fe-Ca-silicates can be
106 associated with magnetite, pyrrhotite, chalcopyrite, pentlandite, sphalerite and isocubanite
107 (Fig. 4B, D, and F). Textural relationships attest for synchronous crystallization of Fe-Ca
108 silicates and sulfides. Locally, magnetite associated with ilvaite displays growth or dendrite-
109 like textures indicative of contemporaneity (Fig. 4G, S1-1).

110 The proportion of magnetite and sulfides increases toward the most mineralized zones,
111 defining an assemblage of semi-massive sulfides. It consists of millimetric to centimetric
112 veins made of pyrrhotite and magnetite in textural equilibrium, minor chalcopyrite and
113 pentlandite and Fe-antigorite/greenalite at their rims (Fig. 4H). Pentlandite has low Ni (21.3 to
114 24.2 wt.%) and low Co (2.9 to 3.6 wt.%) contents (with Co/Ni ratio ~ 0.15 , Fig. 5A).

115 Pyrrhotite displays intermediate Ni contents (average ~ 2800 ppm, Fig. 5C). Secondary
116 oxidation minerals are pyrite/marcasite, violarite, bornite and covellite (Fig. S1-1).

117 In the most mineralized zones, serpentinites are almost completely replaced by a Cu-Fe-Ni-
118 Co-Zn-rich assemblage of euhedral pyrrhotite, magnetite, pentlandite, Fe-diopside and minor
119 small sphalerite enclosed within chalcopyrite (from 20% up to 50% of the mineralization, Cu-
120 rich MS) displaying isocubanite exsolutions. All grains are in apparent textural equilibrium
121 (Fig. 4I). Pentlandite displays low Ni (24.9 to 25.7 wt.%) and high Co (14.1 to 15.3 wt.%)
122 contents (with Co/Ni ratio \sim 0.58, Fig. 5A). Pyrrhotite has low Ni contents ($<$ 2000 ppm,
123 average \sim 720 ppm).

124 Close to the detachment (i.e. Snake Pit), Fe-Ca-silicates are absent. The mineralization
125 consists of disseminated euhedral pyrite grains or aggregates with minor chalcopyrite,
126 pyrrhotite, pentlandite and sphalerite (Fig. 6B). Pentlandite displays high Ni (33 to 33.8 wt.%)
127 and low Co (1.4 to 1.6 wt.%) contents (with Co/Ni ratio \sim 0.05, Fig. 5A). Pyrrhotite has high
128 Ni contents ($>$ 3000 ppm, average about 4700 ppm, Fig. 5C). Steeply-dipping N-S calcite
129 veins crosscut the mineralized serpentinite (Fig. 6A). These carbonates display $\delta^{13}\text{C}$ values
130 from 0.94 to 2.35‰ (Table S3-1, Fig. 6C; full range of the MCHS from -1.28 to 2.35‰) and
131 $\delta^{18}\text{O}$ values from 11.6 to 13.1‰ (full range of the MCHS from 11.5 to 13.1‰). Calcite veins
132 from Snake Pit yield a Jurassic U-Pb age of 144 ± 13 Ma (Fig. 6D).

133 **Discussion**

134 **1) Preservation of the MCHS during the Alpine overprint**

135 A recurrent problem when dealing with rift-related pre-Alpine structures in the Alps is
136 to assess the Alpine tectonic and metamorphic overprint. At Cotschen, the Jurassic
137 detachment and the nearby mineralization associated with dyke-like intrusions were tilted in
138 the footwall of a N-vergent D3 thrust. Because they show roughly the same orientation as the
139 detachment, the intrusions presently in “dyke-like” position were probably sills intruded near-

140 parallel to the detachment and schistose serpentinites. Despite tilting, the intrusions retained
141 their planar attitude, and are crosscut by only a few faults with metric offsets (Figs. 3C, D, F),
142 indicating that the system underwent limited internal strain.

143 In addition, several petrographic and isotopic features show that the system is preserved. First,
144 calcite veins crosscutting the mineralized serpentinite display carbon isotope signatures
145 typical of present-day marine ophicalcites forming at the seafloor (Ribeiro da Costa *et al.*,
146 2008; Bach *et al.*, 2011); their $\delta^{18}\text{O}$ around 12‰ is diagnostic of carbonation at temperatures
147 around 130°C (temperatures already reported along neighboring Jurassic detachment; Coltat
148 *et al.*, 2019). Finally, these carbonates yield a Jurassic U-Pb age (Fig. 6D).

149 **2) The MCHS: a fossil root zone of UHS**

150 The Cu-Fe-Ni-Co-Zn mineralization previously reported in mafic-ultramafic settings
151 worldwide have been attributed to either a magmatic (i.e. orthomagmatic Ni-Cu-PGE and Fe-
152 Ti-V deposits with cumulate and mat textures in mafic-ultramafic intrusions, Foose, 1985;
153 Song *et al.*, 2003) or to a hydrothermal origin (Foose *et al.*, 1985; Thalhammer *et al.*, 1986;
154 Maslennikov *et al.*, 2017). In the present case, the transformation of lizardite into Fe-
155 antigorite/greenalite, the stockwork structures and the metasomatic replacement of
156 serpentinites by ore phases and Fe-Ca-silicates are diagnostic of epigenetic mineralization
157 attesting for a hydrothermal origin.

158 The MCHS presents similarities with the UHS at the MAR (Table 2). Both
159 hydrothermal systems share a geometry implying a detachment fault juxtaposing basalts onto
160 serpentinites (McCaig *et al.*, 2007). Mineralogical similarities are numerous: Cu-Fe-Ni-Co-Zn
161 mineralization of the MCHS is typical of UHS (Fouquet *et al.*, 2010); the replacement
162 textures observed in the Cu-rich MS are expected to occur in the highly altered zones close to

163 seafloor (Marques *et al.*, 2006); the Co enrichment of Cu-rich MS pentlandite is a feature
164 shared with pentlandite from active systems (Mozgova *et al.*, 1996; Borodaev *et al.*, 2007).
165 The presence of mafic intrusions and the lack of hydrothermal chimneys suggest that the
166 MCHS represents the deep levels of an UHS. This is consistent with the limited size of the
167 mineralized bodies when compared to sulfide lenses observed at UHS seafloor. Also, the
168 mineralogical diversity recorded at the MCHS (i.e. Fe-Ca-silicates together with ore minerals)
169 has never been reported for UHS where intensive steatization is rather observed. Similarly,
170 the high and low proportions of magnetite and sphalerite, respectively, slightly contrast with
171 the mineralogical assemblage described for UHS (see Fouquet *et al.*, 2010 for a review, Table
172 2). We therefore propose that the geometric and mineralogical features of the MCHS are
173 symptomatic of UHS root zones.

174 **3) Conceptual model**

175 A conceptual model for the formation of UHS based on this study is proposed in
176 figure 7. During mantle exhumation, downward infiltration of seawater induced pervasive
177 serpentinization of the peridotites (Fig. 7A). The resulting fluids were likely focused all the
178 way to the seafloor along the detachment. The inception and cooling of gabbroic bodies and
179 associated dyke and sill networks at depth likely triggered hydrothermal circulation. Fluids
180 circulated along faults cutting through basalts and into the permeable serpentinite basement
181 where they interacted with rocks (Marques *et al.*, 2006; McCaig *et al.*, 2007) (Fig. 7A). The
182 resulting acidic, reduced and hot black smoker-type fluids reacted with serpentinization-
183 derived fluids to form the mineralogical assemblage reported at the MCHS (Fig. 7A). Upward
184 fluid circulation was enhanced along mafic-ultramafic interfaces; mafic intrusions acted as
185 drains. In the deepest parts, Fe-Ca-silicates crystallized together with ore minerals. In the
186 upper part, close to the detachment (Snake Pit), these silicates were no longer stable, possibly

187 because of the circulation of oxidized seawater that increased f_{O_2} and enhanced pyrite
188 stabilization.

189 On the deepest parts, the mineralogical zonation from barren serpentinite to Fe-Ca-silicates to
190 semi-massive sulfides and then to Cu-rich MS (Figs. 3E, 7B) has never been reported before
191 this study. The ilvaite-andradite-diopside assemblage has been described in low-grade
192 metamorphic serpentinites (Agata and Agachi, 1995) and in oceanic ultramafic settings
193 (Gaggero *et al.*, 1995). Gaggero *et al.* (1995) suggested that this assemblage precipitated from
194 early serpentinization-derived fluids. Gustafson (1974) showed that the ilvaite-hedenbergite-
195 andradite-magnetite assemblage is stable at low f_{O_2} (10^{-25} to 10^{-32}), high-T ($425 \pm 75^\circ\text{C}$)
196 conditions without strong changes if considering diopside instead of hedenbergite. In parallel,
197 the semi-massive sulfides and Cu-rich MS mineralogy suggests precipitation from acidic,
198 reduced and hot ($>350^\circ\text{C}$) fluids, which would have probably interacted with mafic rocks
199 (McCaig *et al.*, 2007) as well as ultramafic rocks to explain Ni enrichment. These conditions
200 are compatible with those forming Fe-Ca-silicates as the formation of hydrated minerals (e.g.
201 ilvaite, hydroandradite and actinolite) decreases the pH of the fluid (Allen and Seyfried,
202 2003). In addition, CH_4 - and H_2 -rich venting fluids reported for UHS (Charlou *et al.*, 2002)
203 suggest that concomitant in-depth serpentinization occurred during black-smoker-related
204 hydrothermal activity. We thus propose that the horizontal zonation observed at depth results
205 from increasing fluid/rock ratios from the outer zones to the stockwork zone then to the most
206 mineralized zones.

207 Finally, the cooling of the system is recorded through Late Jurassic hydrothermal carbonation
208 ($\sim 130^\circ\text{C}$) close to the detachment plane. Previous studies have emphasized that carbonation
209 could derive from the mixing between serpentinization-derived uprising fluids (along the
210 detachment) and seawater close to the seafloor (Kelley *et al.*, 2001; Ludwig *et al.*, 2006). The
211 $\delta^{13}\text{C}$ values of the MCHS opicalcites are similar to those reported at the Lost-City

212 hydrothermal field suggesting that the same mechanism could have caused carbonate
213 precipitation in the MCHS.

214 **Conclusions**

215 The distribution of mineralized assemblages across the Marmorera-Cotschen Hydrothermal
216 System records the subsurface evolution of an ultramafic-hosted hydrothermal system, from a
217 Cu-Fe-Ni-Co-Zn-rich assemblage and associated Fe-Ca-silicates in the deepest zones to a
218 sulfide-rich, silicate-free mineralization close to the detachment plane. Carbonation marked
219 the end of the hydrothermal circulation. The MCHS formed in a hyper-extended margin. This
220 suggests that black smoker-type hydrothermal activity is not restricted to oceanic domains but
221 can also occur in Ocean-Continent Transitions, which should lead us to reconsider metal
222 resources available in such geodynamic settings.

223 **Acknowledgments**

224 The authors would like to thank J. Langlade for help with microprobe analyses, X. Lecoq for
225 the preparation of thin sections. We acknowledge Andrew Martin and one anonymous
226 reviewer for their constructive reviews. This study was founded through CNRS-INSU and
227 University of Rennes 1 “D efis Scientifiques” grants (accorded to P. Boulvais and R. Coltat).

228 **References**

- 229 Agata, T., and Adachi, M., 1995. Ilvaite from a serpentinized peridotite in the Asama igneous
230 complex, Mikabu greenstone belt, Sambagawa metamorphic terrain, central Japan:
231 *Mineralogical Magazine*, **59**, 489-496.
- 232 Allen, D. E., and Seyfried, W. E., 2003. Compositional controls on vents fluids from
233 ultramafic-hosted hydrothermal systems at mid-ocean ridges: an experimental study at 400 C,

- 234 500 bars: *Geochimica et Cosmochimica Acta*, **67**, 1531-1542, doi:10.1016/S0016-
235 7037(02)01173-0
- 236 Alt, J.C., Crispini, L., Gaggero, L., Levine, D., Lavagnino, G., Shanks, P., and Gulbransen,
237 C., 2018. Normal faulting and evolution of fluid discharge in a Jurassic seafloor ultramafic-
238 hosted hydrothermal system: *Geology*, **46**, 523-526, doi:org/10.1130/G40287.1
- 239 Bach, W., Rosner, M., Jöns, N., Rausch, S., Robinson, L.F., Paulick, H., and Erzinger, J.,
240 2011. Carbonate veins trace seawater circulation during exhumation and uplift of mantle rock:
241 Results from ODP Leg 209: *Earth and Planetary Science Letters*, **311**, 242-252,
242 doi:10.1016/j.epsl.2011.09.021
- 243 Bill, M., O'Dogherty, L., Guex, J., Baumgartner, P. O., and Masson, H., 2001. Radiolarite
244 ages in Alpine-Mediterranean ophiolites: Constraints on the oceanic spreading and the
245 Tethys-Atlantic connection: *Geological Society of America Bulletin*, **113**, 129-143,
246 doi:10.1130/00167606(2001)113<0129:RAIAMO>2.0.CO;2
- 247 Boillot, G., et al., 1987. Tectonic denudation of the upper mantle along passive margins; a
248 model based on drilling results (ODP Leg 103, western Galicia margin, Spain):
249 *Tectonophysics*, **132**, 335-342, doi:10.1016/0040-1951(87)90352-0
- 250 Borodaev, Y. S., Bryzgalov, I. A., Mozgova, N. N., and Uspenskaya, T., Y., 2007. Pentlandite
251 and Co-enriched pentlandite as characteristic minerals of modern hydrothermal sulphide
252 mounds hosted by serpentinitized ultramafic rocks (Mid-Atlantic Ridge): *Moscow University*
253 *Geological Bulletin*, **62**, 85-97, doi:10.3103/S0145875207020032
- 254 Bortnikov, N.S., Vikentyev, I. V., Apollonov, V. N., Stavrova, O. O., Bogdanov, Y. A., Lein,
255 A. Y., Gurvich, E. G., Sagalevich, A. M., Simonov, V. A., and Ikorskii, S. V., 2001. The
256 Rainbow serpentinite-hosted hydrothermal field, Mid-Atlantic Ridge, 36°14'N: Mineralogical
257 and geochemical features: *Mineral Deposits at the Beginning of the 21st Century*, 265-268

- 258 Charlou, J. L., Donval, J. P., Fouquet, Y., Jean-Baptiste, P., and Holm, N., 2002.
259 Geochemistry of high H₂ and CH₄ vent fluids issuing from ultramafic rocks at the Rainbow
260 hydrothermal field (36°14'N, MAR): *Chemical Geology*, **191**, 345-359, doi:10.1016/S0009-
261 2541(02)00134-1
- 262 Coltat, R., Boulvais, P., Branquet, Y., Collot, J., Epin, M.E., and Manatschal, G., 2019. Syn-
263 tectonic carbonation during syn-magmatic mantle exhumation at an ocean-continent
264 transition: *Geology*, **47**, 183-186, <https://doi.org/10.1130/G45530.1>
- 265 Desmurs, L., Müntener, O., and Manatschal, G., 2002. Onset of magmatic accretion within a
266 magma-poor rifted margin: a case study from the Platta ocean-continent transition, eastern
267 Switzerland: *Contrib. Mineral. Petrol.*, **144**, 365-382. doi:10.1007/s00410-002-0403-4
- 268 Dietrich, V., 1972, Die sulfidischen Vereezungen in den Oberhalbsteiner Serpentiniten:
269 *Geotechnische Serie*, **49**, 129pp.
- 270 Douville, E., Charlou, J.L., Oelkers, E.H., Bienvenu, P., Jove Colon, C.F., Donval, J.P.,
271 Fouquet, Y., Prieur, D., and Appriou, P., 2002. The rainbow vent fluids (36°14'N, MAR): the
272 influence of ultramafic rocks and phase separation on trace metal content in Mid-Atlantic
273 Ridge hydrothermal fluids: *Chemical Geology*, **184**, 37-48.
- 274 Dunoyer de Segonzac, G., and Bernoulli, D., 1976. Diagenèse et métamorphisme des argiles
275 dans le Rhétien Sud-Alpin et Austro-alpin (Lombardie et Grisons): *Bulletin de la Société*
276 *géologique de France*, **18**, 1283-1293.
- 277 Epin, M.E., 2017. Evolution morpho-tectonique et magmatique polyphasée des marges ultra-
278 distales pauvres en magma : la transition océan-continent fossile de l'Err et de la Platta (SE
279 Suisse) et comparaison avec des analogues actuels, Unpubl. doctoral dissertation, Université
280 de Strasbourg, Strasbourg, 340pp.

- 281 Evrard, C., Fouquet, Y., Moëlo, Y., Rinert, E., Etoubleau, J., and Langlade, J. A., 2012. Tin
282 concentration in hydrothermal sulphides related to ultramafic rocks along the Mid-Atlantic
283 Ridge: a mineralogical study: *Eur. J. Mineral.*, **27**, 627-638, doi:10.1127/ejm/2015/0027-2472
- 284 Ferreiro Mählmann, R., 1994. Zur Bestimmung von Diagenesehöhe und beginnender
285 Metamorphose: Temperaturgeschichte und Tektogenese des Austroalpins und
286 Südpenninikums in Vorarlberg und Mittelbünden, Institut für Geochemie, Petrologie und
287 Lagerstättenkunde der Johann Wolfgang Goethe Universität.
- 288 Firstova, A., Stepanova, T., Cherkashov, G., Goncharov, A., and Babaeva, S., 2016.
289 Compositions and formation of gabbro-peridotite hosted seafloor massive sulfide deposits
290 from the Ashadze-1 hydrothermal field, Mid-Atlantic Ridge: *Minerals*, **19**, 20pp,
291 doi:10.3390/min6010019
- 292 Foose, M. P., 1985. The setting of a magmatic sulfide occurrence in a dismembered ophiolite,
293 southwest Oregon: *U.S. Geol. Surv. Bull.*, **1626A**
- 294 Foose, M. P., Economou, M., and Panayiotou, A., 1985. Compositional and mineralogic
295 constraints on the genesis of ophiolitic hosted nickel mineralization in the Pevkos area,
296 Limassol forest, Cyprus: *Mineralium Deposita*, **20**, 234-240
- 297 Fouquet, Y., et al., 2008. Serpentine Cruise – ultramafic hosted hydrothermal deposits on the
298 Mid-Atlantic Ridge: First submersible studies on Ashadze 1 and 2, Logatchev 2 and Krasnov
299 vents fields: *InterRidge News*, **17**, 16-21
- 300 Fouquet, Y., et al., 2010. Geodiversity of hydrothermal processes along the Mid-Atlantic
301 Ridge and ultramafic-hosted mineralization: a new type of oceanic Cu-Zn-Co-Au
302 volcanogenic massive sulphide deposit: *Geophysical Monograph Series*, **188**, 321-367

- 303 Froitzheim, N., Schmid, S. M., and Conti, P., 1994. Repeated change from crustal shortening
304 to orogen-parallel extension in the Austroalpine units of Graubünden: *Eclogae Geologicae*
305 *Helveticae*, **87/2**, 559-612, doi.org/10.5169/seals-167471
- 306 Froitzheim, N., and Manatschal, G., 1996. Kinematics of Jurassic faulting, mantle
307 exhumation, and passive-margin formation in the Austroalpine and Penninic nappes (eastern
308 Switzerland): *GSA Bulletin*, **108**, 1120-1133
- 309 Gaggero, L., Cortesogno, L., and Gazzoti, M., 1997. Data Report: Oxides, sulphides and
310 associated phases in veins and hydrothermally altered peridotitic rocks. In: *Proceedings of the*
311 *Ocean Drilling Program* (Karson, J.A., Cannat, M., Miller, D.J., and Elthon, D.). *Scientific*
312 *Results*, **153**, 523-529
- 313 Goodfellow, W. D., and Franklin, J. M., 1993. Geology, mineralogy, and chemistry of
314 sediment-hosted clastic massive sulfides in shallow cores, Middle Valley, Northern Juan de
315 Fuca Ridge: *Economic Geology*, **88**, 2037-2068
- 316 Gustafson, W. I., 1974. The stability of andradite, hedenbergite and related minerals in the
317 system Ca-Fe-Si-O-OH: *Journal of Petrology*, **15**, 455-96
- 318 Hannington, M. D., Tivey, M. K., Larocque, A. C. L., Petersen, S., and Rona, P. A., 1995.
319 The occurrence of gold in sulfide deposits of the TAG hydrothermal field, Mid-Atlantic
320 Ridge: *Can. Mineral.*, **33**, 1285-1310.
- 321 Herzig, P.M., Petersen, S., and Hannington, M., 1998. Geochemistry and sulfur-isotopic
322 composition of the TAG hydrothermal mound, Mid-Atlantic Ridge, 26°N': *Proceedings of*
323 *the Ocean Drilling Program, Scientific Results*, **158**, 47-70
- 324 Kelley, D. S., et al., 2001. An off-axis hydrothermal vent field near the Mid-Atlantic Ridge at
325 30°N: *Nature*, **412**, 145-149.

- 326 Ludwig, K. A., Kelley, D. S., Butterfield, D. A., Nelson, B. K., and Früh-Green, G., 2006.
327 Formation and evolution of carbonate chimneys at the Lost City hydrothermal field:
328 *Geochimica et Cosmochimica Acta*, **70**, 3625-3645, doi:10.1016/j.gca.2006.04.016
- 329 Marques, A.F.A., Barriga, F., Chavagnac, V., and Fouquet, Y., 2006. Mineralogy,
330 geochemistry and Nd isotope composition of the Rainbow hydrothermal field, Mid-Atlantic
331 Ridge: *Mineralium Deposita*, **41**, 52-67, DOI 10.1007/s00126-005-0040-8
- 332 Maslennikov, V. V., et al., 2017. Chimneys in Paleozoic massive sulfide mounds of the Urals
333 VMS deposits: Mineral and trace element comparison with modern black, grey, white and
334 clear smokers: *Ore Geology Reviews*, **85**, 64-106, doi:10.1016/j.oregeorev.2016.09.012
- 335 McCaig, A.M., Cliff, R.A., Escartin, J., Fallick, A.E., and McLeod, C.J., 2007. Oceanic
336 detachment faults focus large volumes of black smoker fluids: *Geology*, **35**, 935-938,
337 doi:10.1130/G23657A
- 338 McCaig, A.M., Delacour, A., Fallick, A.E., Castelain, T., and Gretchen, F.G., 2010.
339 Detachment fault control on hydrothermal circulation systems: interpreting the subsurface
340 beneath the TAG hydrothermal field using the isotopic and geological evolution of oceanic
341 core complexes in the Atlantic: *Geophysical Monograph Series*, **188**, 207-239
- 342 Mozgova, N. N., Krasnov, S. G., Batuyev, B. N., Borodaev, Y. S., Efimov, A. V., Markov, V.
343 F., and Stepanova, T., V., 1996. The first report of cobalt pentlandite from a Mid-Atlantic
344 Rige hydrothermal deposit: *The Canadian Mineralogist*, **34**, 23-28.
- 345 Nehlig, P., and Marquez, L., 1998. Feeder zones of massive sulfide deposits: Constraints from
346 Bent Hill, Juan de Fuca Ridge – ODP Leg 169: *Water-rock interaction*, 751-754
- 347 Nickel, E. H., Ross, J. R., and Thornber, M. R., 1974. The supergene alteration of pyrrhotite-
348 pentlandite ore at Kambalda, Western Australia: *Economic Geology*, **69**, 93-107.

- 349 Ondreas, H., Cannat, M., Fouquet, Y., and Normand, A., 2012. Geological context and vents
350 morphology of the ultramafic-hosted Ashadze hydrothermal areas (Mid-Atlantic Ridge
351 13°N): *Geochemistry, Geophysics, Geosystems*, **13**, 20pp, doi:10.1029/2012GC004433
- 352 Pinto, V. H. G., Manatschal, G., Karpoff, A. M., and Viana, A., 2015. Tracing mantle-reacted
353 fluids in magma-poor rifted margins: the example of Alpine Tethyan rifted margins:
354 *Geochemistry, Geophysics, Geosystems*, **16**, 3271-3308, doi:10.1002/2015GC005830.
- 355 Ribeiro da Costa, I., Barriga, F. J. A. S., and Taylor, R. N., 2008. Late seafloor carbonate
356 precipitation in serpentinites from the Rainbow and Saldanha sites (Mid-Atlantic Ridge): *Eur.*
357 *J. Mineral.*, **20**, 173-181, doi:10.1127/0935-1221/2008/0020-1803
- 358 Rona, P. A., and Scott, S. D., 1993. A special issue on sea-floor hydrothermal mineralizations:
359 new perspectives: *Economic Geology*, **88**, 1935-1976
- 360 Schaltegger, U., Desmurs, L., Manatschal, G., Müntener, O., Meier, M., Frank, M., and
361 Bernoulli, D., 2002. The transition from rifting to sea-floor spreading within a magma-poor
362 rifted margin: field and isotopic constraints: *Terra Nova*, **14**, 156-162, doi:10.1046/j.1365-
363 3121.2002.00406.x
- 364 Song, X.-Y., Zhou, M.-F., Cao, Z.-M., Sun, M., and Wang, Y.-L., 2003. Ni-Cu-(PGE)
365 magmatic deposits in the Yangliuping area, Permian Emeishan igneous province, SW China:
366 *Mineralium Deposita*, **38**, 831-943, doi:10.1007/s00126-003-0362-3
- 367 Thalhammer, O., Stumpfl, E. F., and Panayiotou, A., 1986. Postmagmatic, hydrothermal
368 origin of sulfide and arsenide mineralizations at Limassol forest, Cyprus: *Mineralium*
369 *Deposita*, **21**, 95-105

370 Tucholke, B. E., Lin, J., and Kleinrock, M. C., 1998. Megamullions and mullion structure
371 defining oceanic metamorphic core complexes on the Mid-Atlantic Ridge: *Journal of*
372 *Geophysical Research*, **103**, 9857-9866

373 **Figure captions**

374 Figure 1. (A) Simplified genetic model proposed for the formation of active ultramafic-hosted
375 black-smokers deposits (e.g. Rainbow-type systems) along slow-spreading ridges showing the
376 speculated fluid pathway (after McCaig *et al.*, 2007). Seawater percolates through fractures
377 and faults crosscutting the mafic cover and circulates through the permeable serpentinite
378 basement where it gets heated in the vicinity of the gabbroic intrusions before rising up in the
379 serpentinized footwall. The fluid thus discharges the metals by mixing with cold seawater.
380 NVZ=Neo Volcanic Zone. (B) Seafloor expression of hydrothermal venting activity at the
381 Rainbow field (2200 m.b.s.l., photo from Ifremer).

382 Figure 2. (A) Simplified map of the main paleogeographic units of the Central and Western
383 Alps and the Apennines. (B) Geological map of the Platta nappe (modified after Schaltegger
384 *et al.*, 2002) showing the Marmorera-Cotschen area (black inset). (C) Reconstructed cross
385 section shows mantle exhumation beneath the Adriatic plate during the Jurassic WNW-ESE-
386 oriented opening of the Alpine Tethys Ocean (after Pinto *et al.*, 2015). Mantle exhumation
387 recorded in the Platta nappe was accommodated by detachment faults and was accompanied
388 by mafic magmatism (gabbros, dolerites and basalts). As a consequence of a low magmatic
389 budget, large parts of the seafloor expose mantle rocks without the establishment of a
390 Penrose-type oceanic crust.

391 Figure 3. (A) General view of the cliff of the Marmorera-Cotschen hydrothermal system. The
392 mineralization is distributed almost continuously from the Marmorera Lake (bottom of the
393 picture, 1684m above sea level (m.a.s.)) up to Cotschen (2308 m.a.s.) exposing about 600m of

394 vertical relief. (B) Line-drawing of the picture displayed in (A) At most places, the
395 serpentinite-hosted mineralization occurs as thin corridors (up to several meters) while the
396 main gossan has a width of 90 meters. (C) Relationship between dyke-like south-dipping
397 mafic intrusions and mineralization in the upper gossan. Mineralization is hosted in the
398 serpentinite on the southern flank of each intrusion, resulting in a repeated S-N spatial
399 sequence of mineralized serpentinite, the mafic intrusion and barren serpentinite (grassy
400 areas). (D) Actinolite-rich (Act) alteration at a mafic intrusion - mineralized serpentinite
401 interface in the upper gossan. (E) On the margin of mafic intrusions intruding the serpentinites
402 at Marmorera, occurrence of a hydrothermal zonation evolving from Cu-rich massive sulfide
403 (Cu-rich MS) and semi-massive sulfide to barren serpentinite. (F) Top-to-the-NNW reverse
404 fault (D3 Alpine phase) displacing by a few meters a planar mafic intrusion in the upper
405 gossan.

406 Figure 4. Micrographs illustrating the mineralogical evolution from the barren serpentinites to
407 the Cu-rich MS (i.e. approaching the mafic intrusions). (A) Barren serpentinite exhibiting
408 early small ($< 50\mu\text{m}$) magnetite (Mt I) and pentlandite (Pn I) grains along serpentine (Srp I)
409 grain boundaries and within serpentine domains, respectively. Location in figure 3E. (B)
410 Ilvaite (Ilv) and Fe-diopside (Dp) veins enclosing chalcopyrite (Cp) and magnetite (Mt II)
411 grains from a Fe-Ca-silicates stockwork structure. Some magnetite grains are also found in
412 the serpentine groundmass without specific relationship to Fe-Ca-silicates. (C) Typical Fe-Ca-
413 silicates stockwork structure cutting through serpentinites. (D) Zoom on the internal
414 composition of the stockwork shown in figure 4C. It consists of ilvaite (Ilv) and minor Fe-
415 diopside (Dp) veins. The serpentine groundmass contains small disseminated grains or
416 aggregates of sphalerite and pentlandite (Pn + Sp). Smaller sulfide grains ($< 25 \mu\text{m}$, not
417 visible on that scale) are also present in the Fe-Ca-silicates veins, which suggests that sulfides
418 formed before the silicate stockwork. Spinel (Spn) relics persist in the serpentine groundmass.

419 (E) Extensive metasomatic replacement of serpentinite by Fe-Ca-silicates and associated
420 sulfides and oxides. (F) Sulfide aggregate made of sphalerite (Sp), chalcopyrite (Cp) with
421 isocubanite (Is) exsolutions, and magnetite (Mt II). The aggregate is surrounded by an
422 assemblage of magnetite, hydroandradite (Adr) and ilvaite (Ilv). White arrows point to
423 dendritic-like intergrowths of magnetite and ilvaite, suggesting a concomitant crystallization
424 of the two phases. (G) Growth texture attesting for a synchronous crystallization of magnetite
425 (Mt II) and ilvaite (Ilv). Chalcopyrite (Cp) is locally present within ilvaite. (H) Semi-massive
426 sulfide made of magnetite (Mt II) and pyrrhotite (Po) veins associated with a newly formed
427 serpentine phase (Srp II, likely Fe-antigorite or greenalite). Location in figure 3E. (I) Cu-rich
428 massive sulfides with an assemblage made of chalcopyrite (Cp) with isocubanite (Is)
429 exsolutions, pyrrhotite (Po), magnetite (Mt II), pentlandite (Pn II) and Fe-diopside (Dp)
430 enclosing serpentine clasts (Srp II). Location in figure 3E.

431 Figure 5. Elemental discriminant diagrams for pentlandite (A) and magnetite (B) grains from
432 the MCHS and present-day occurrences at the MAR. (A) Co vs. Ni (wt. %) diagram for
433 pentlandite from the MCHS plotted together with Co-rich pentlandite from seafloor Cu-rich
434 chimneys at the MAR (Mozgova *et al.*, 1996). The increase in intensity of the hydrothermal
435 alteration intensity increase is marked an increase of the Co/Ni ratio. The loss of Ni in
436 pentlandite from semi-massive sulfides likely reflects the alteration of pentlandite into
437 violarite (Nickel *et al.*, 1974). (B) Si (ppm) vs. Fe (wt. %) diagram for magnetite from
438 Marmorera and magnetite from the Rainbow hydrothermal field (this study). Compared to
439 syn-serpentinization magnetite (green squares, $4000 < \text{Si} < 13000$ ppm), syn-mineralization
440 magnetite (all other squares) has lower Si contents (< 6200 ppm, average around 1900 ppm).
441 (C) Frequency histogram of Ni content (ppm) for pyrrhotite from the MCHS. The mean
442 composition of several pyrrhotite grains from different hydrothermal assemblages of Rainbow
443 (MAR) is also shown (Marques *et al.*, 2006). A negative correlation between the Ni content of

444 pyrrhotite and the intensity of the hydrothermal alteration is visible in both the active (i.e.
445 Rainbow) and fossil (i.e. MCHS) systems.

446 Figure 6. Features associated with carbonation in the serpentinites right beneath the Jurassic
447 detachment (Snake Pit and Marmorera outcrops, located in figure 3A and B). (A) Mineralized
448 serpentinite crosscut by sub-vertical calcite veins. (B) Pyrite (Py) + chalcopyrite (Cp)
449 aggregate hosted in serpentine (Srp) and crosscut by late calcite (Cc). (C) $\delta^{13}\text{C}$ vs. $\delta^{18}\text{O}$
450 isotopic diagram of ophicalcites from the MCHS and present-day marine ophicalcites from
451 the 15°20'N Fracture Zone at MAR (Bach *et al.*, 2011). $\delta^{13}\text{C}$ signatures of the ophicalcites
452 from the MCHS overlap with those from the MAR. In contrast, $\delta^{18}\text{O}$ signatures of the
453 ophicalcites from the MCHS are much lower than those from the MAR, reflecting different
454 temperatures of formation for the two systems. (D) Tera-Wasserburg diagram for calcite
455 grains from sample Cot16_49 at Snake Pit (LA-ICP-MS U-Pb analyses). The analyses are
456 discordant and lie on a linear trend with a lower intercept date at 144 ± 13 Ma. Ellipsoids are
457 displayed with a confidence of $\pm 2\sigma$.

458 Figure 7. (A) Genetic model for the formation of the MCHS before carbonation hydrothermal
459 stage. During mantle exhumation along a detachment, seawater percolates downward through
460 the faulted mafic hangingwall and the damaged serpentinite footwall where it leaches metals
461 (the exact sources need further investigation). The heat transferred from cooling of shallow
462 gabbroic bodies triggers hydrothermal convection. The fluids get heated and rise in the
463 damage zone of the detachment likely up to the surface where metal deposition from the
464 fluids form UHS. Fluid circulation is guided by lithological interfaces such as the contacts
465 between mafic intrusions and serpentinites. Synchronously, at greater depth, active
466 serpentinization of peridotite releases fluids which, on their way to the surface, likely mix
467 with black smoker-type fluids, forming the mineralogical assemblage reported in this study.
468 (B) Schematic view of the mineralogical zonation occurring on the margin of mafic dykes,

469 ranging from barren serpentinite to an envelope of Fe-Ca-silicates stockwork, to semi-massive
470 sulfides and ultimately Cu-rich MS. The transition between fresh lizardite-rich serpentinite
471 and the Fe-Ca-silicates stockwork is marked by the replacement of lizardite by a Fe-rich
472 serpentine (likely Fe-antigorite). The overall zonation likely reflects an increase of the
473 fluid/rock ratio from the outer parts (i.e. barren serpentinite) to the inner part (i.e. Cu-rich MS)
474 of the system.

Table 2. Main characteristics of present-day and fossil oceanic hydrothermal systems

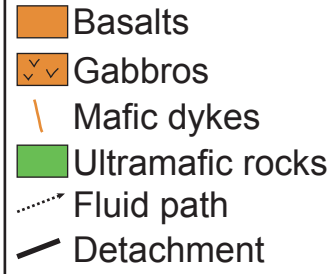
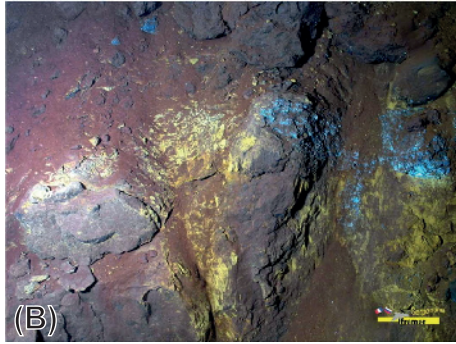
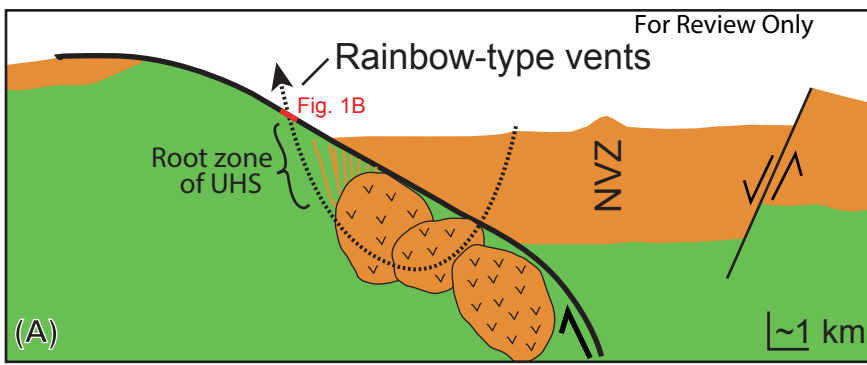
Hydrothermal system	Rainbow	Logatchev 1	Ashadze 1	TAG	Bent-Hill	Fossil MCHS (this study)
Location	MAR 36°14'N	MAR 14°45'N	MAR 12°58'N	MAR 26°08'N	Middle Valley rift; N Juan de Fuca Ridge	Platta nappe, Swiss Alps
Host rocks	Serpentinite	Serpentinite	Serpentinite	MORB	Turbidites	Serpentinite
Mineralization type	Cu-Zn-Co-Au	Cu-Zn-Fe-Ni-Co	Zn-Cu-Fe-Ni-Co	Fe-Zn-Cu	Fe-Cu-Zn	Cu-Fe-Ni-Co-Zn
Tectonic setting	Nontransform offset, ultramafic dome	East valley wall	West rift valley wall, detachment fault	Rift wall, volcanic centers	Rift valley	Serpentinized detachment footwall
Type of mineralization	Chimneys + MS	Mound + chimneys	Chimneys + MS	Mound	Chimneys + MS	Stockwork + MS
Size (m)	400 x 100	400 x 150	200	250 x 250 x 45	400 x 400 x 60	90 x 90 (max.)
Main hydrothermal phases	Is, Cp, Sp, Po, Pn, Au	Cp, Is, Sp, Py, Pn	Cp, Sp, Is, Po, Bn	Py, An, Cp, (Sp)	Py, Po, Cp, Sp	Cp, Po, Mt , Ilv , Ad , Dp , Pn, Is, Sp
References	Fouquet et al., 2010; Marques et al., 2006; Charlou et al., 2002; Bortnikov et al., 2001	Fouquet et al., 2010; Evrard et al., 2015; Fouquet et al., 2008	Fouquet et al., 2010; Fouquet et al., 2008; Ondreas et al., 2012; Firstova et al., 2016	Fouquet et al., 2010; Herzig et al., 1998; Rona and Scott, 1993; Hannington et al., 1995	Nehlig and Marquez, 1998; Goodfellow and Franklin, 1993	Dietrich, 1972; This study

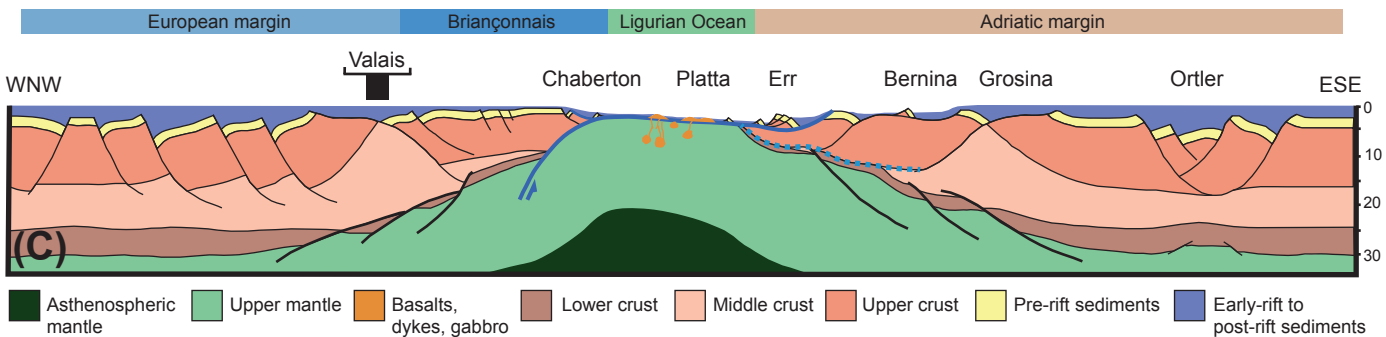
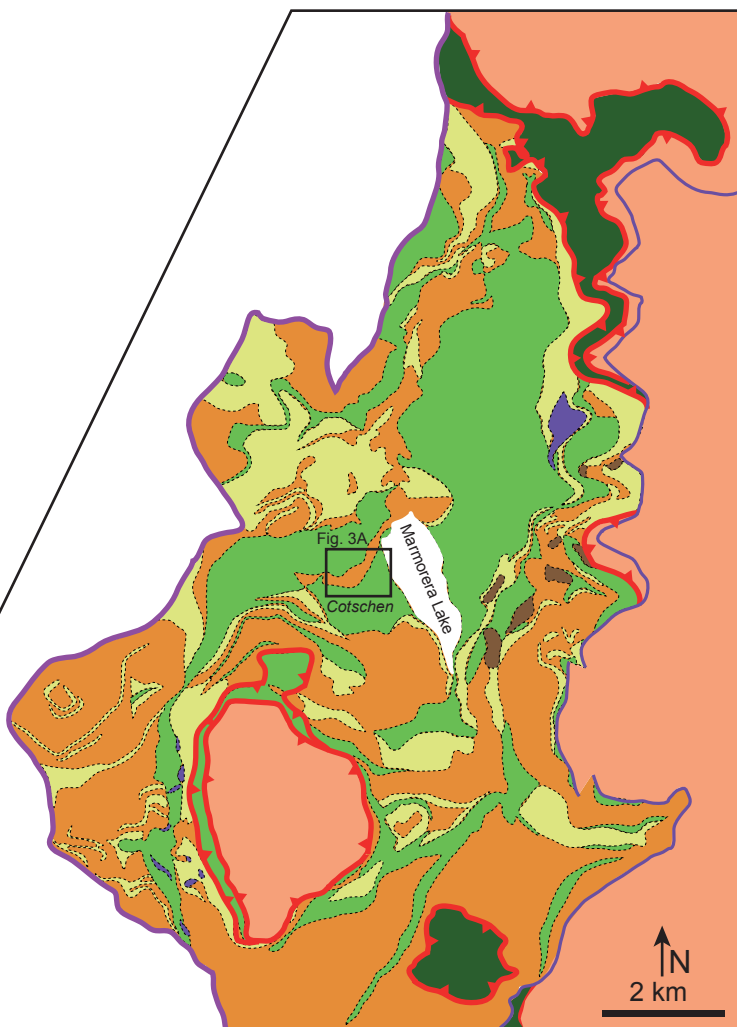
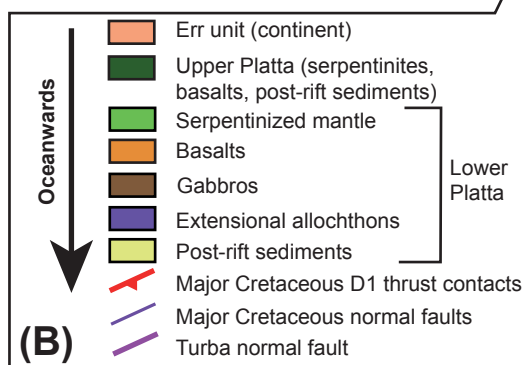
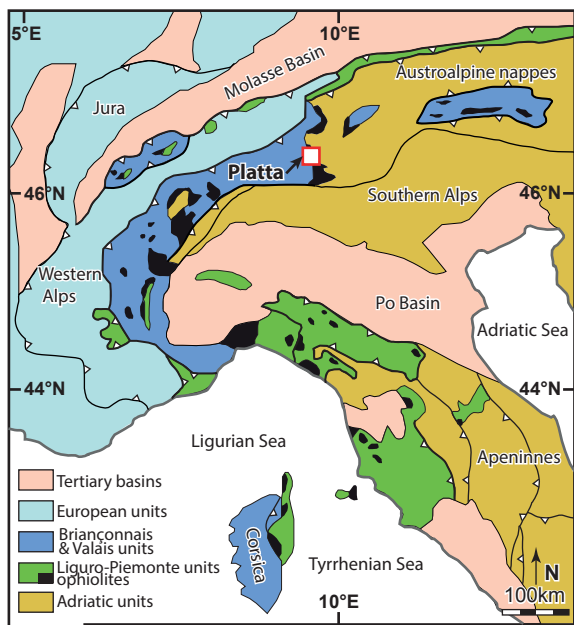
In **bold** are displayed the hydrothermal phases which differ from present-day systems

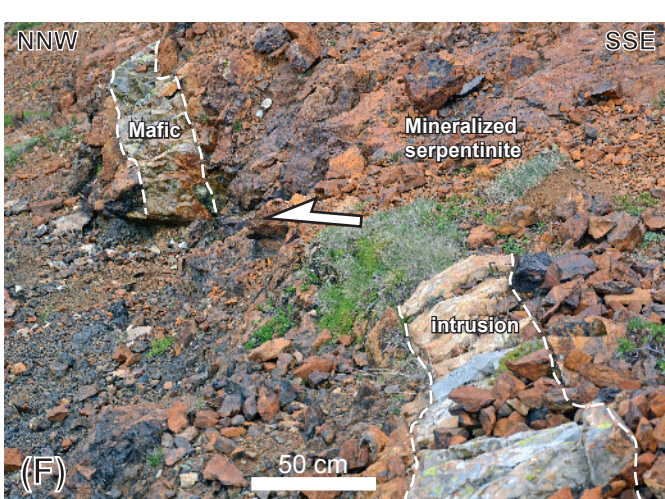
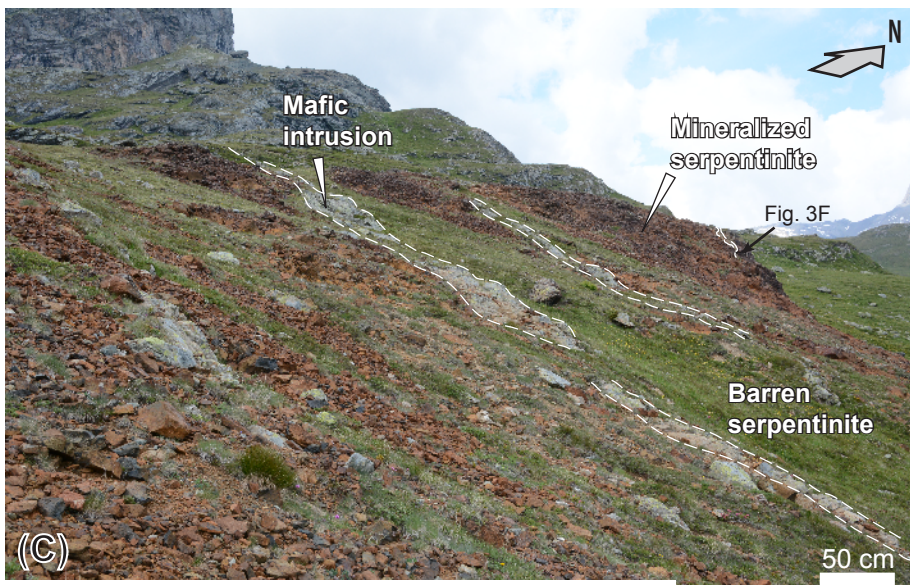
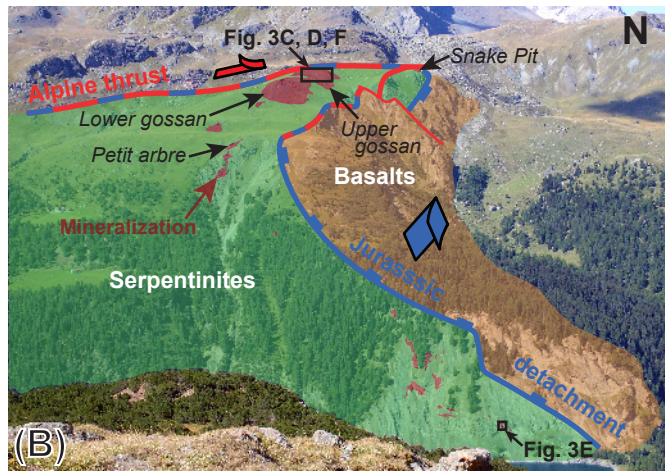
The elements displayed in the mineralization type are given by modal abundance

Is=isocubanite, Cp=chalcopyrite, Sp=sphalerite, Po=pyrrhotite, Pn=pentlandite, Py=pyrite, Bn=bornite, An=anhydrite, Mt=magnetite, Ilv=ilvaite, Ad=hydroandradite, Dp=diopside, MS=massive sulphide

For Review Only







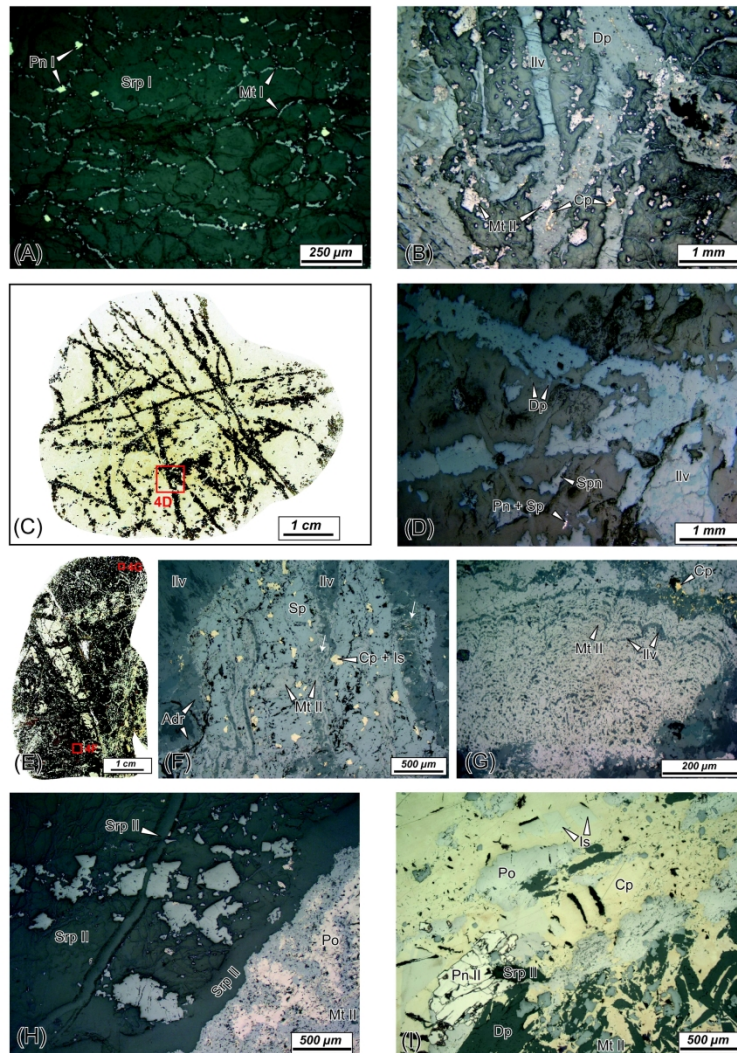


Figure 4. Micrographs illustrating the mineralogical evolution from the fresh serpentinites to the Cu-rich MS (i.e. approaching the mafic intrusions). (A) Fresh serpentinite exhibiting early small ($< 50\mu\text{m}$) magnetite (Mt I) and pentlandite (Pn I) grains along serpentine (Srp I) grain boundaries and within serpentine domains, respectively. Location in figure 3E. (B) Ilvaite (Ilv) and Fe-diopside (Dp) veins enclosing chalcopyrite (Cp) and magnetite (Mt II) grains from a Fe-Ca-silicates stockwork structure. Some magnetite grains are also found in the serpentine groundmass without specific relationship to Fe-Ca-silicates. (C) Typical Fe-Ca-silicates stockwork structure cutting through serpentinites. (D) Zoom on the internal composition of the stockwork shown in figure 4C. It consists of ilvaite (Ilv) and minor Fe-diopside (Dp) veins. The serpentine groundmass contains small disseminated grains or aggregates of sphalerite and pentlandite (Pn + Sp). Smaller sulfide grains ($< 25\mu\text{m}$, not visible on that scale) are also present in the Fe-Ca-silicates veins, which suggests that sulfides formed before the silicate stockwork. Spinel (Spn) relics persist in the serpentine groundmass. (E) Extensive metasomatic replacement of serpentinite by Fe-Ca-silicates and associated sulfides and oxides. (F) Sulfide bleb made of sphalerite (Sp), chalcopyrite (Cp) with isocubanite (Is) exsolutions, and magnetite (Mt II). The bleb is surrounded by an assemblage of magnetite,

hydroandradite (Adr) and ilvaite (Ilv). White arrows point to dendritic-like intergrowths of magnetite and ilvaite, suggesting a concomitant crystallization of the two phases. (G) Growth texture attesting for a synchronous crystallization of magnetite (Mt II) and ilvaite (Ilv). Chalcopyrite (Cp) is locally present within ilvaite. (H) Semi-massive sulfide (SMS) made of magnetite (Mt II) and pyrrhotite (Po) veins associated with a newly formed serpentine phase (Srp II, likely Fe-antigorite or greenalite). Location in figure 3E. (I) Cu-rich massive sulfides with an assemblage made of chalcopyrite (Cp) with isocubanite (Is) exsolutions, pyrrhotite (Po), magnetite (Mt II), pentlandite (Pn II) and Fe-diopside (Dp) enclosing serpentine clasts (Srp II). Location in figure 3E.

209x296mm (300 x 300 DPI)

